ACS APPLIED MATERIALS & INTERFACES

Research Article

www.acsami.org

Thermoelectric Power Generation from Lanthanum Strontium Titanium Oxide at Room Temperature through the Addition of Graphene

Yue Lin,[†] Colin Norman,[†] Deepanshu Srivastava,[†] Feridoon Azough,[†] Li Wang,[†] Mark Robbins,[‡] Kevin Simpson,[‡] Robert Freer,*[,†] and Ian A. Kinloch*[,†]

[†]The School of Materials, University of Manchester, Oxford Road, Manchester M13 9PL, United Kingdom

[‡]European Thermodynamics Ltd, 8 Priory Business Park, Kibworth, Leicester LE8 0RX, United Kingdom

Supporting Information

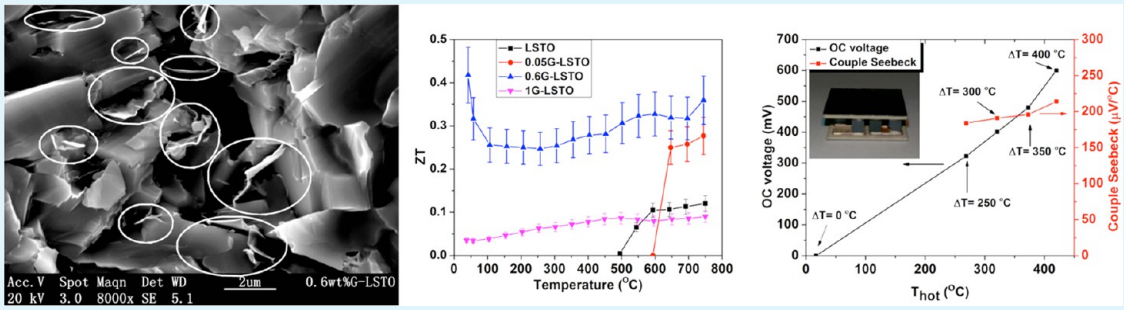

ABSTRACT: The applications of strontium titanium oxide based thermoelectric materials are currently limited by their high operating temperatures of >700 °C. Herein, we show that the thermal operating window of lanthanum strontium titanium oxide (LSTO) can be reduced to room temperature by the addition of a small amount of graphene. This increase in operating performance will enable future applications such as generators in vehicles and other sectors. The LSTO composites incorporated one percent or less of graphene and were sintered under an argon/hydrogen atmosphere. The resultant materials were reduced and possessed a multiphase structure with nanosized grains. The thermal conductivity of the nanocomposites decreased upon the addition of graphene, whereas the electrical conductivity and power factor both increased significantly. These factors, together with a moderate Seebeck coefficient, meant that a high power factor of ~2500 $\mu Wm^{-1} K^{-2}$ was reached at room temperature at a loading of 0.6 wt % graphene. The highest thermoelectric figure of merit (ZT) was achieved when 0.6 wt % graphene was added (ZT = 0.42 at room temperature and 0.36 at 750 °C), with >280% enhancement compared to that of pure LSTO. A preliminary 7-couple device was produced using bismuth strontium cobalt oxide/graphene-LSTO pucks. This device had a Seebeck coefficient of ~1500 μV/K and an open voltage of 600 mV at a mean temperature of 219 °C.

KEYWORDS: *graphene, bulk strontium titanate, environmental friendly, high thermoelectric performance, broad thermal window*

INTRODUCTION

Currently, about two-thirds of the energy generated from hydrocarbon sources, such as oil and gas, is lost as waste heat.[1,2] To improve energy efficiency and reduce carbon dioxide emissions, there is increasing interest in high performance thermoelectric materials to harvest some of this waste energy.[1−5] Thermoelectric materials are able to directly convert heat to electrical energy via the Seebeck effect, in which an electromotive force develops when the materials are located in a temperature gradient. Thermoelectric power generation is a rapidly growing sector with applications in many areas including automotive, aerospace, heavy manufacturing industries, and remote power generation.[1,5−7] The efficiency of a thermoelectric material is characterized by the dimensionless figure of merit (ZT), which is defined as $ZT = (S^2\sigma/\kappa)T$, where S, σ, κ, and T are the Seebeck coefficient, electrical conductivity, thermal conductivity, and temperature, respectively. A number of high ZT metallic thermoelectric materials have been developed in the past three decades such as tellurium (Te)-based compounds[2,3,8] and selenium (Se)-based compounds.[4,9] However, these materials are usually too heavy, expensive, or toxic to find universal application, particularly when the environmental impact is considered.[5] Furthermore, they are limited in their ability to harvest electricity at high temperatures, such as from solar and industrial waste heat, due to their decomposition and volatilization at elevated temperatures.[5,10,11] Over the past decade, there has been growing interest in alternatives to these alloys, and this interest has led to the development of oxide-based materials.[5] Recent reviews[5,6,12−14]

Received: April 23, 2015
Accepted: June 22, 2015
Published: June 22, 2015

ACS Publications © 2015 American Chemical Society

DOI: 10.1021/acsami.5b03522
ACS Appl. Mater. Interfaces 2015, 7, 15898−15908

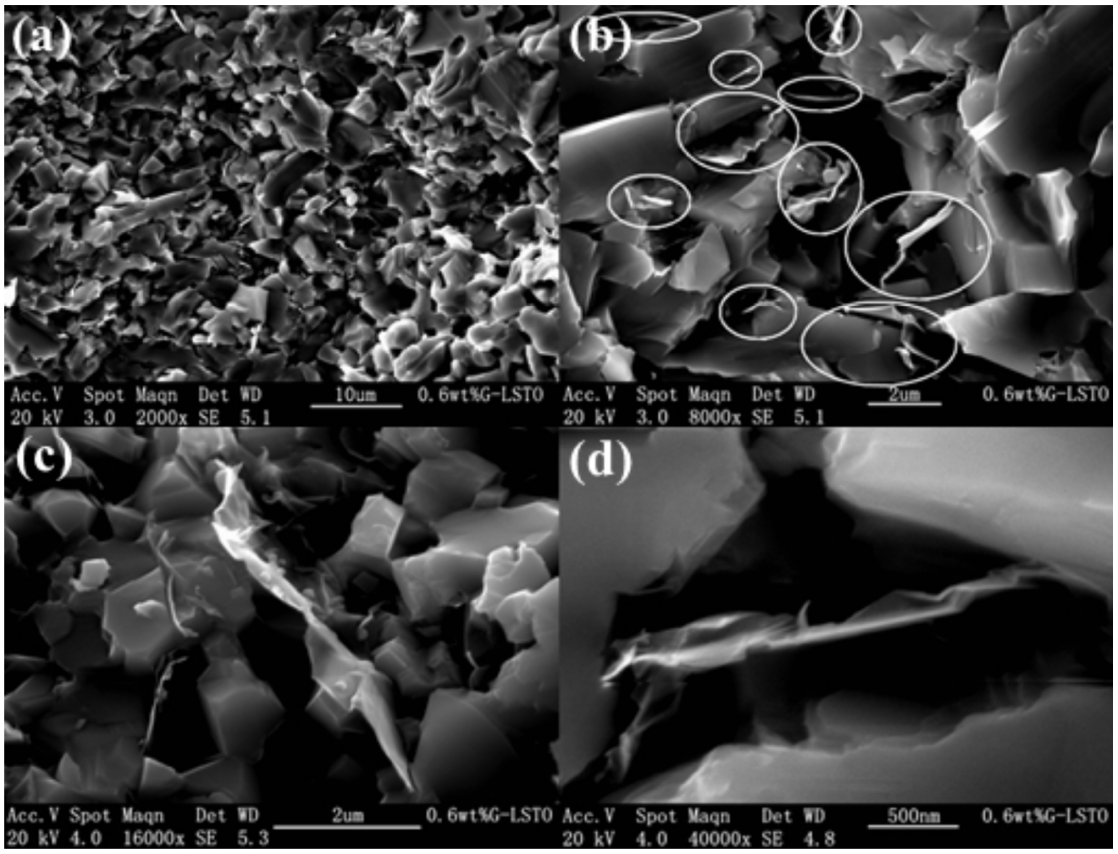

Figure 1. SEM images of the fracture surface of 0.6 wt % G/LSTO nanocomposites (a) at low magnification, (b) at high magnification, and (c, d) showing morphology of the graphene sheets.

have highlighted the potential of a range of oxides including those based on $SrTiO_3$, ZnO, TiO_2, $CaMnO_3$, and $Ca_3Co_4O_9$.

The perovskite-type strontium titanate ($SrTiO_3$) has attracted significant interest owing to its large carrier effective mass, good thermal stability at high temperature, and strong structural tolerances for substitutional doping.[6] A popular route for enhancing the thermoelectric performance of $SrTiO_3$, which is poor in its intrinsic form, is to increase its electrical conductivity by doping. $SrTiO_3$ can be easily modified by doping with either trivalent elements (e.g., Lanthanum (La) and dysprosium (Dy)) at the Sr sites,[15,16] and pentavalent elements (e.g., Niobium (Nb)) at the Ti sites.[17−19] Additionally, efforts have been made to reduce the thermal conductivity while preserving the electrical conductivity.[7] In the $SrTiO_3$ system, reduction of the thermal conductivity has been achieved by creating oxygen vacancies,[20] nanostructuring,[21,22] and inclusion of fillers with low thermal conductivity.[23] Wang et al.[15] doped $SrTiO_3$ with La and Dy using a conventional solid-state reaction method. The power factor (defined as $S^2\sigma$) reached 1318 $\mu W/K^2$ m, and a ZT of 0.36 was obtained at 803 °C with 12% Dy and 8% La doping. Dang et al.[21] prepared self-assembled particulate films from La-$SrTiO_3$ nanocubes, with assistance of UV irradiation. After calcination at 1000 °C under a reducing atmosphere, the film exhibited a Seebeck coefficient of −239 μV/K, electrical conductivity of 160 S/cm, and low thermal conductivity of 1.5 W/mK, which resulted in a high ZT value of 0.2 at room temperature compared with that of 0.08 for a La-$SrTiO_3$ single crystal with similar composition.

Although significant progress has been made in the enhancement of the thermoelectric performance of $SrTiO_3$, major challenges remain. The critical parameters of S, σ, and κ are interdependent, which complicates the efforts to improve the average ZT of the material. The thermoelectric properties of $SrTiO_3$ continue to be inferior to those of the traditional metal materials. This low ZT has restricted the commercial application of oxide-based materials. Thus, $SrTiO_3$ based thermoelectric materials with higher ZT are desirable. Furthermore, thermoelectric materials have a "thermal window" within which they are able to convert heat energy into electrical energy, effectively an operating range within which the materials display useful properties. Outside this temperature range, which is unique to any particular material, the material has little or no ability to generate electrical energy in response to heat. Consequently, the exploitation of these materials in different applications is limited not only by their ZT values, but also by the range of temperature within which they operate. Very few of the existing thermoelectric materials exhibit a broad thermal window, for example, from room temperature to 750 °C. Thus, for a typical thermoelectric device employed in dynamic thermal conditions, the performance is never optimal. For conditions with large temperature variations, thermoelectric materials with different thermal windows are assembled together (so-called "cascade" structure) to fabricate a suitable thermoelectric device, which complicates the fabrication process and significantly increases cost. Therefore, the synthesis of a material with a broad thermal window or a technique that can produce this kind of material is vitally important to optimize device performance and simplify device integration. The formulation we selected $La_{0.67}Sr_{0.9}TiO_3$ was based on the earlier work on La doped strontium titanates[12,24] and was

DOI: 10.1021/acsami.5b03522
ACS Appl. Mater. Interfaces 2015, 7, 15898−15908

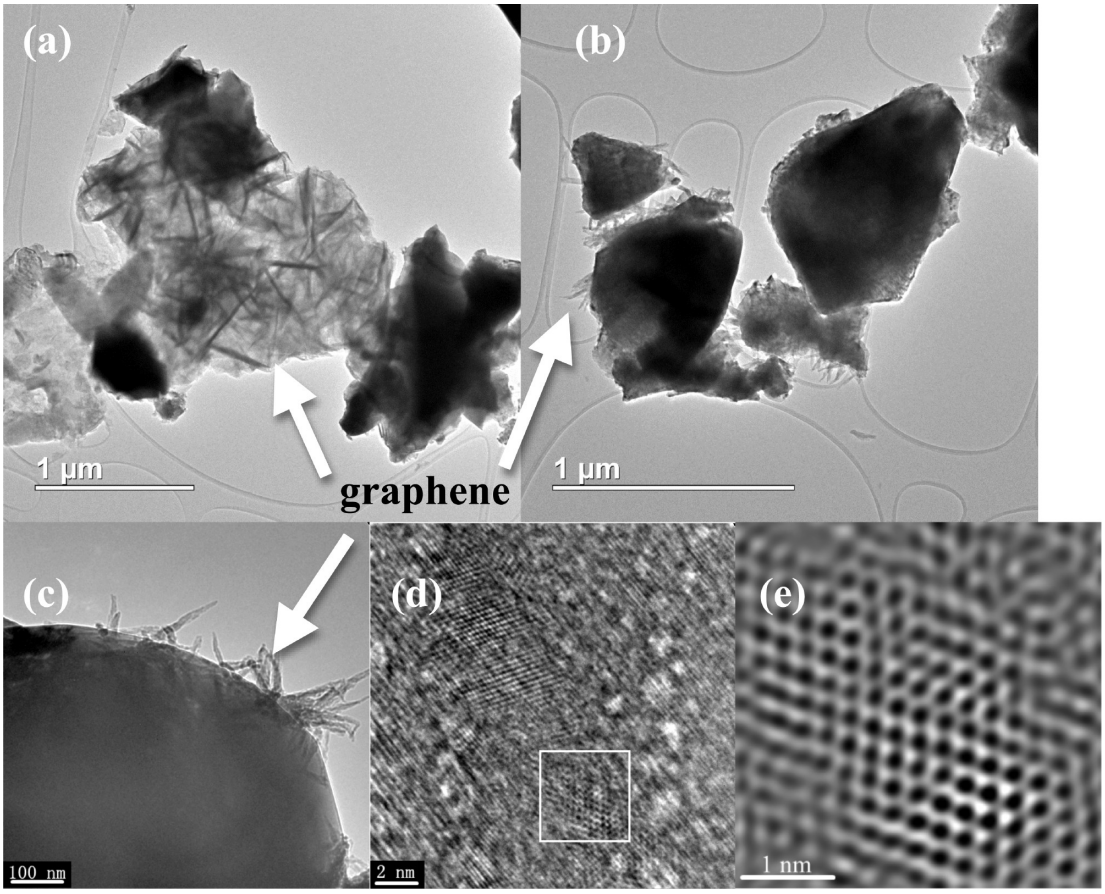

Figure 2. TEM images of a crushed 0.6 wt % G/LSTO nanocomposite. (a) Multilayer graphene sheets containing LSTO grains, (b) crushed grains with graphene at the edges, (c) grain-edged view in high magnification, (d) high-resolution (HR)TEM image of graphene at the edge of a grain, and (e) HRTEM image of the graphene region identified by the white square marked in panel d.

optimized following trial investigations. It provides the simplicity of charge balance for standard oxidation states, but phonon scattering by A-site vacancies under reduced conditions.

Graphene has attracted much attention because of its unique and valuable properties.[25−27] It has been reported that graphene has a giant Seebeck coefficient of 30 mV/K,[28] charge carrier mobility of over 2×10^5 $cm^2/(V\ s)$,[29] electrical conductivity of above 10^6 S/m,[30] as well as extraordinary electronic transport properties.[31−33] With these exceptional properties, graphene has considerable potential as second phase to enhance the thermoelectric properties of existing thermal and electric materials, in particular through the improvement of the charge carrier conductivity. The incorporation of graphene has shown improvements in metal[34,35] and polymer[36−38] based thermoelectric materials. However, the application of graphene in oxide-based materials, such as $SrTiO_3$, has not to the authors' knowledge been investigated before. Herein, we report new thermoelectric behavior for bulk graphene/lanthanum strontium titanium oxide (LSTO) nanocomposites. Rather than working within a narrow "thermal window", these nanocomposites exhibit useful *ZT* values across a broad temperature range of several hundred degrees. The thermoelectric performance is further demonstrated in a prototype 7-couple device. This discovery highlights an alternative strategy to nanostructuring for developing high-performance, environmental friendly, and low cost bulk thermoelectric materials. It may provide the foundation for the application of thermoelectric devices based on metal oxides and new design strategies.

RESULTS AND DISCUSSION

Microstructural Analysis. Raman spectroscopy (Figure S1, Supporting Information) showed that the graphene was typically a few layers thick and survived the composite sintering process, with little structural change. Scanning electron microscopy (SEM) of the graphene/LSTO (G/LSTO) nanocomposites revealed that the graphene was dispersed at the edges of the ceramic grains without any obvious localized aggregation (Figure 1). Transmission electron microscopy (TEM) showed that the LSTO grains were covered by a mixture of multilayer graphene sheets (Figure 2a,b) and thinner graphene flakes, which were stabilized by curling at their edges (Figure 2c). High-resolution imaging of these sheets showed the characteristic hexagonal atomic symmetry of graphene (Figure 2d,e).

Electron backscattered diffraction (EBSD) demonstrated that the LSTO grain size decreased significantly with increased concentration of graphene (Figure 3). For the pure LSTO (Figure 3d), the average grain size was 2.2 μm, with a largest grain size of ∼10 μm, and no grains smaller than 1 μm. However, upon the addition of 0.1 wt % graphene (Figure 3e), the average grain size remained around a micron (1.2 μm), but over 53% of grains were nanosized (<1 μm). For the 0.6 wt % G/LSTO (Figure 3f), the calculated average grain size was 412 nm, which is about five-times smaller than that of pure LSTO.

DOI: 10.1021/acsami.5b03522
ACS Appl. Mater. Interfaces 2015, 7, 15898−15908

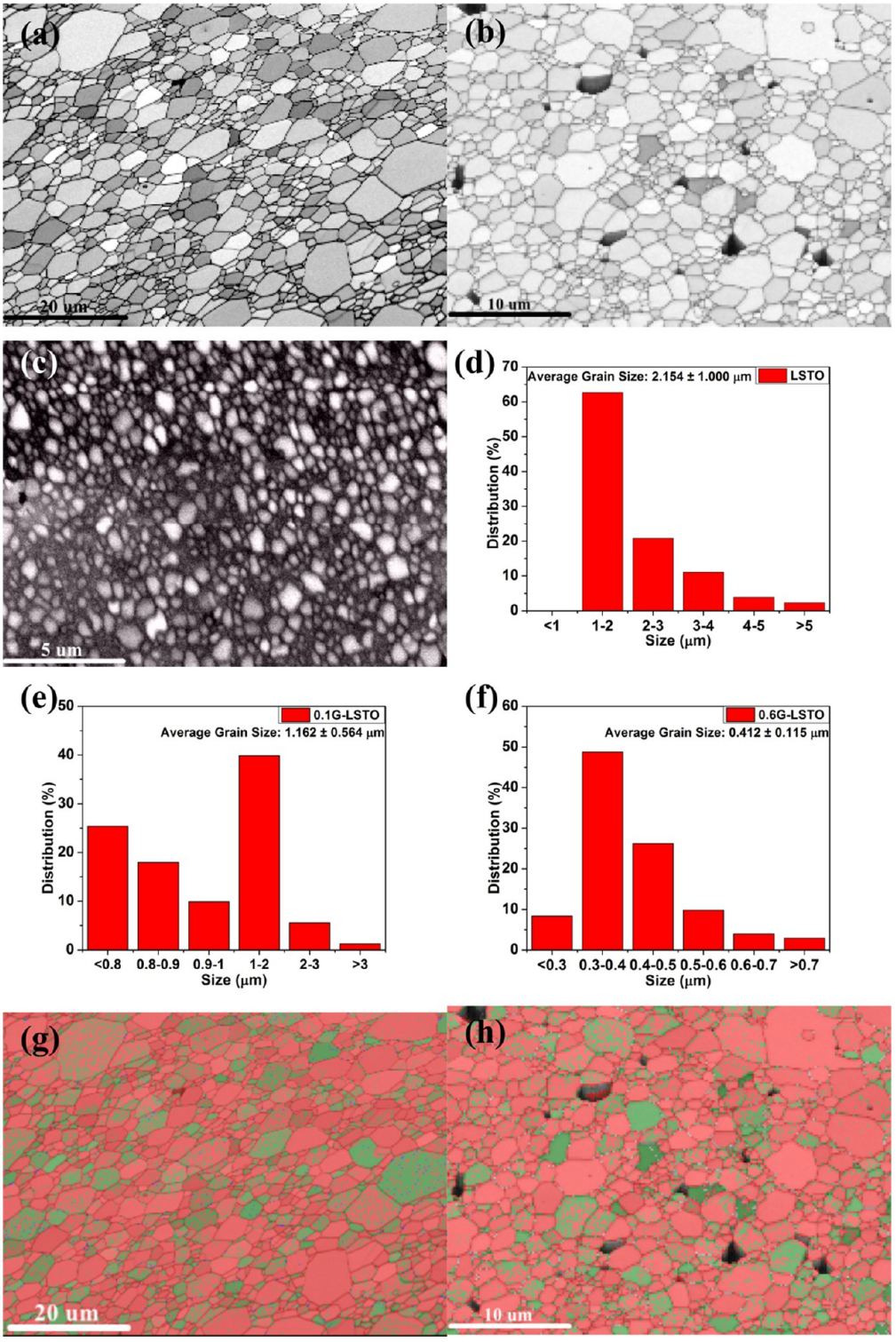

Figure 3. EBSD analysis of LSTO and its nanocomposite with graphene. (a) Band contrast image of pure LSTO, (b) band contrast image of 0.1 wt % G/LSTO, (c) band contrast image of 0.6 wt % G/LSTO, (d) grain size distribution of pure LSTO, (e) grain size distribution of 0.1 wt % G/LSTO, (f) grain size distribution of 0.6 wt % G/LSTO, (g) color phase image of pure LSTO (the red color indicates a tetragonal phase, and the green color indicates a cubic phase), and (h) color phase image of 0.1 wt % G/LSTO, with phases as indicated in panel g.

Furthermore, the largest grain size in the 0.6 wt % G/LSTO was only ~1 μm. The densities for the LSTO and all the G/LSTO composites were above 97% of the theoretical density (see Table S2 in Supporting Information). Thus, considering the limited influence of graphene concentration on the bulk density, it is believed that the presence of graphene acted as a nucleating agent during sintering. The phase purities of the pure and graphene-doped samples were similar, showing the presence of both (i) the *P*4/*mmm* tetragonal structure (red in Figure 3g,h) and (ii) the *Pm*-3m cubic structure (green in Figure 3 g,h). It is plausible, based upon the X-ray diffraction (XRD) data, that the former phase is $SrTiO_{2.6}$, which is very

DOI: 10.1021/acsami.5b03522
ACS Appl. Mater. Interfaces 2015, 7, 15898−15908

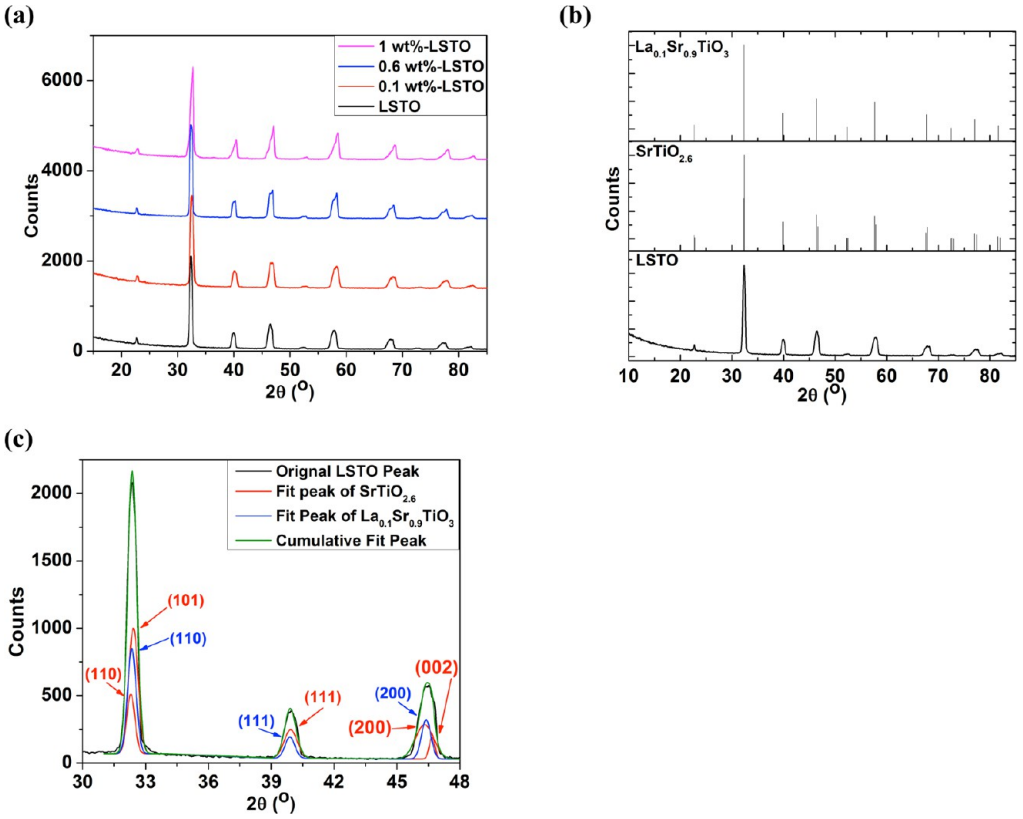

Figure 4. XRD spectra for LSTO and its nanocomposites: (a) overview, (b) comparison of LSTO with reference files, and (c) detail of spectra showing three major diffraction peaks in LSTO.

Table 1. Structural Parameters for the Phases in LSTO

crystal system	space group	relative formula	a (Å)	c (Å)	% phases[a]	cell mass	cell volume (Å^3)
cubic	*Pm*-3m	$La_{0.067}Sr_{0.9}TiO_3$	3.8903		32.4	161.096	58.878
tetragonal	*P*4/*mmm*	$La_{0.067}Sr_{0.9}TiO_{2.6}$	3.9253	3.9073	67.6	191.008	60.205

[a]Calculated proportion of phases in LSTO ceramics from Rietveld analysis.

similar to the base composition of $La_{0.067}Sr_{0.9}TiO_{2.6}$, and the latter is $La_{0.1}Sr_{0.9}TiO_{3.0}$, which is very similar to the composition $La_{0.067}Sr_{0.9}TiO_{3.0}$.

XRD showed that the LSTO possessed the *Pm*-3m space group symmetry (Figure 4a,b), and this was unchanged by the addition of graphene. Furthermore, the diffraction peaks are broad, which implies a range of grain sizes or compositions. Analysis of the XRD data was carried out by fitting the diffraction peaks using Topas. Data for $La_{0.1}Sr_{0.9}TiO_3$ (PDF card No. 01−079−0177),[39] having a similar composition to LSTO, were employed as reference, as there is no direct reference file for the composition used. A magnified section of the pattern is presented in Figure 4, panel c, and the results of the analysis are listed in Table 1. The XRD data strongly suggest the presence of a phase with a tetragonal symmetry, as found in the EBSD results. This tetragonal phase is believed to be due to a reduced phase, and a range of different phases was fitted using the $SrTiO_{3-\delta}$ PDF reference cards on the basis that their structures will be very similar to that of $La_{0.067}Sr_{0.9}TiO_{3-\delta}$, for which no cards exist. The best fit was found to for $La_{0.067}Sr_{0.9}TiO_{2.6}$ (PDF reference card, $SrTiO_{2.6}$ No. 01−080−1935).[40] This fitted phase has an unexpected high degree of reduction, with a δ of 0.4, where typically one would expect $\delta \approx 0.1$. Thermogravimetric analysis was conducted (not shown) with the aim of establishing whether the δ could be measured through the increase in mass from oxidation. However, no significant oxidation within error could be found, which suggests that the δ was indeed closer to 0.1 than 0.4. Rietveld analysis indicates that about 67.6% of the phases in LSTO ceramics are in the reduced state. Hence, the XRD results also imply a combination of a reduced LSTO phase and a strontium lanthanum titanate phase, which is consistent with the EBSD analysis.

Thermoelectric Characterization. The electrical conductivity of the LSTO and selected nanocomposites as a function of temperature is shown in Figure 5, panel a. The behavior of all the samples was found to be reproducible and similar on heating and cooling. The pure LSTO (Figure 5a) showed semiconductive behavior. At low temperatures, the conductivity was very low, but the conductivity increased dramatically with temperature from 500 °C, peaking at 600 °C, and then decreased gradually. The nanocomposites incorporated with 0.05 wt % graphene followed a similar trend, but with higher initiation temperature and maximum conductivity. It is believed at this very low loading, that the resistance of the LSTO phase increased due a combination of the graphene-induced nanotexturing of the composite's grains (Figure 3) and the graphene concentration being too low to sufficiently improvement the conductivity of the composite to offset this grain effect. However, there was a transition in behavior when

DOI: 10.1021/acsami.5b03522
ACS Appl. Mater. Interfaces 2015, 7, 15898−15908

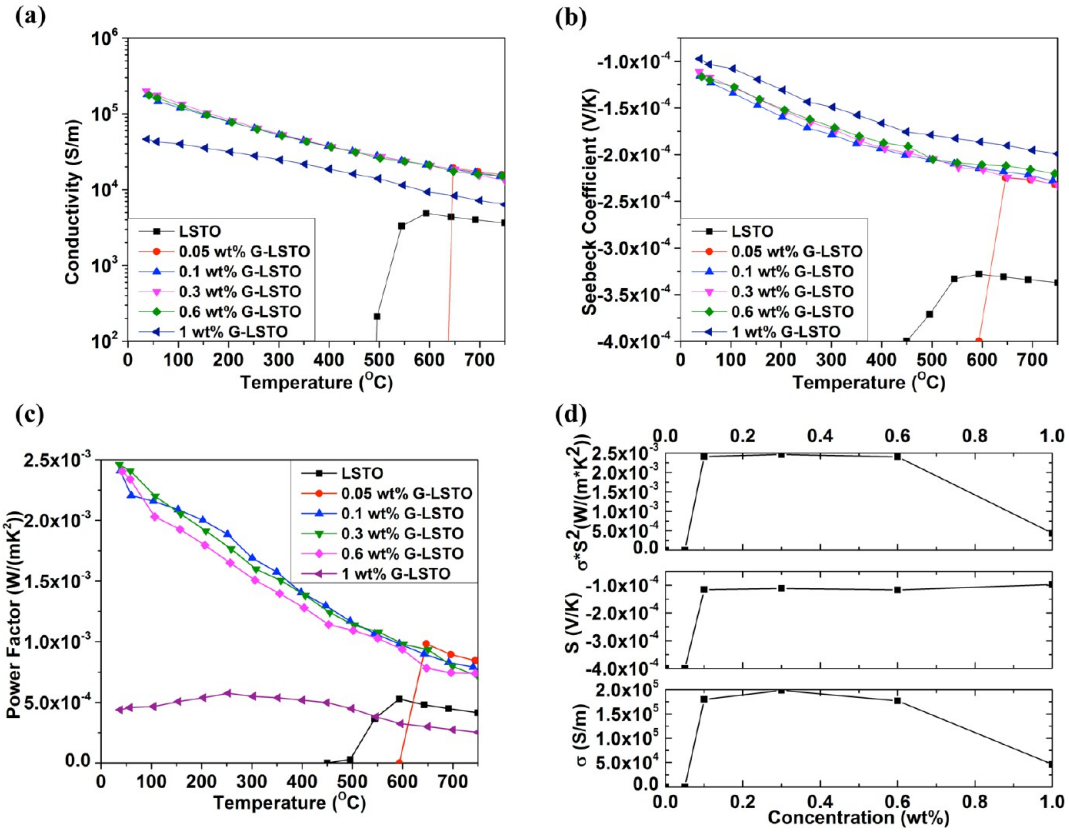

Figure 5. Thermoelectric properties of LSTO and its nanocomposites with graphene: (a) electrical conductivity as a function of temperature, (b) Seebeck coefficient as a function of temperature, (c) power factor as a function of temperature, and (d) electrical conductivity, Seebeck coefficient, and power factor against concentration of graphene at room temperature. The lines are drawn as a guide to the eye. Note that there is a 5% uncertainty in all data points.

0.1 wt % graphene was added. In this case, the nanocomposite had a high electrical conductivity (1.8×10^5 S/m) at room temperature, which gradually decreased with temperature to 0.15×10^5 S/m at 750 °C. Very similar behavior was observed for nanocomposites prepared with 0.3 and 0.6 wt % graphene. The highest electrical conductivity of 2.0×10^5 S/m was reached at room temperature with nanocomposites prepared with the addition of 0.3−0.6 wt % graphene. Nevertheless, the addition of 1 wt % graphene led to a reduction in electrical conductivity by about one order of magnitude compared to that of nanocomposites prepared with lower concentrations. The increase in conductivity with graphene loading may be due to the formation of a percolation network or the graphene facilitating a partial reduction of the LSTO at the grain boundaries, resulting in faster electronic transport. In the case of the former, the percolation threshold would be relatively low since, as previously noted, the graphene is segregated to the grain boundaries. Hence, the network would not be a true random space filling network as in a polymer composite but rather a network that has considerably recduced free volume. The change in behavior at higher loadings may be due to the aggregation of graphene at high concentrations ≥ 1 wt %.

The temperature dependence of the Seebeck coefficients is shown in Figure 5, panel b. All the Seebeck coefficients were negative for LSTO and its nanocomposites with graphene, which indicated n-type electrical conduction behavior. The temperature dependence of the Seebeck coefficient was the converse of that for electrical conductivity. In general, the Seebeck coefficients decreased as the electrical conductivity increased. For pure LSTO, the Seebeck coefficients are between −337 μV/K and −400 μV/K. With the addition of 0.1 wt % graphene, the Seebeck Coefficients fell to −122 μV/K at room temperature and then gradually increased to −228 μV/K with increasing temperature. The 0.3 wt % G/LSTO and 0.6 wt % G/LSTO samples showed very similar trends. While data for the 1 wt % G/LSTO nanocomposite also exhibited a similar trend, the absolute Seebeck coefficient values are significantly lower than those for nanocomposites prepared with lower graphene concentrations. This implies the formation of a carbon network when the concentration of graphene reaches 1 wt %, where the charge carriers travel only through the network rather than both the ceramic matrix and the graphene. This behavior degrades the performance, which indicates that there is an optimum range for graphene additions.

The power factor is shown as a function of temperature in Figure 5, panel c. For LSTO, the highest power factor of 528 μWm^{-1} K^{-2} was achieved at 600 °C. In contrast, for nanocomposites prepared with graphene concentrations of 0.1 wt % to 0.6 wt %, the power factor ranges from 2500−716 μWm^{-1} K^{-2} and decreases with increasing temperature. The higher values resulted from the combination of high electrical conductivity and moderate Seebeck coefficient. Although the power factor of the 1 wt % G/LSTO nanocomposites was modest at room temperature, the performance was inferior to that of LSTO above 600 °C. The composition dependence at room temperature of the electrical conductivity, Seebeck coefficient, and power factor as a function of graphene concentration is summarized in Figure 5, panel d. It is clear

DOI: 10.1021/acsami.5b03522
ACS Appl. Mater. Interfaces 2015, 7, 15898−15908

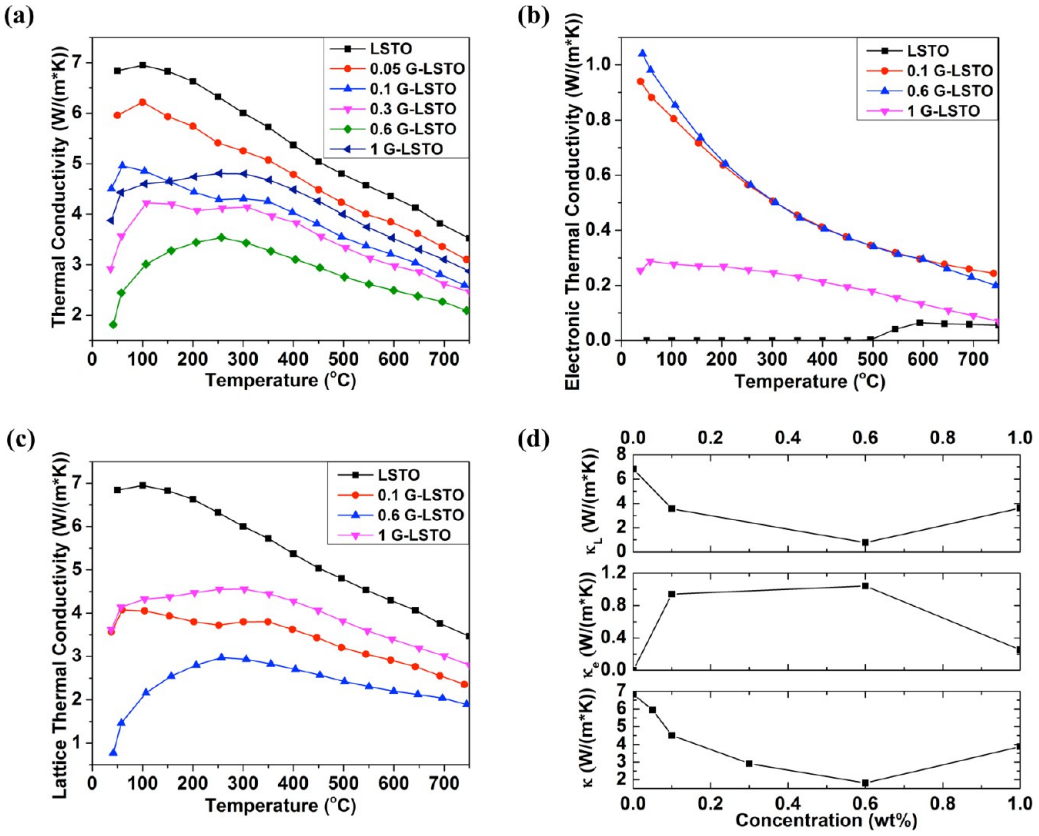

Figure 6. Thermal conductivity of LSTO and its nanocomposites with graphene: (a) total thermal conductivity as a function of temperature. Note that the experimental uncertainty in these points is 10%. (b) Electronic thermal conductivity as a function of temperature, (c) lattice thermal conductivity as a function of temperature, and (d) thermal conductivity at room temperature as a function of graphene concentration. The lines are drawn as a guide to the eye. Note that there is a 10% uncertainty in all data points.

that the addition of graphene led to a significant improvement in properties, but a high loading of graphene ($\geq$ 1 wt %) did not result in any further enhancement.

The total thermal conductivity (κ) of LSTO and the nanocomposites is shown as a function of temperature in Figure 6, panel a. Data for all the samples followed a similar trend; the thermal conductivity increased with temperature or initiated at the maximum value and then dropped. The thermal conductivities of the nanocomposites were found to decrease with increase of graphene content; the conductivity of the 0.6 wt % graphene sample was only 25% of that for pure LSTO. Significantly, this decrease in thermal conductivity was found to occur across the full temperature window (room temperature to 750 °C). One might initially expect the thermal conductivity to increase upon the addition of graphene due to its much higher thermal conductivity than LSTO. However, the graphene used here was in the form of flakes, which means that they have a substantially lower conductivity in the composite due to the scattering at the flake boundaries. More significantly, though, is the previously discussed nanotexturing of the LSTO upon the addition of the graphene (Figure 3). This reduction of the average grain size to <500 nm introduces significant lattice scattering and hence reduces the thermal conductivity of the composite. This reduction from the LSTO dominated over any improvement due to the graphene. This effect of graphene has also been seen in other metallic thermoelectric systems.[34,35]

The electronic thermal conductivity (κ_e) was calculated using Wiedenmann–Franz relation, following the approach of Biswas et al.[2] using the method and calculated data given Supporting Information. Figure 6, panel b shows the resulting calculated electronic thermal conductivity as a function of temperature. The electronic thermal conductivity of pure LSTO is lower than 0.1 $Wm^{-1} K^{-1}$ and increased with the addition of graphene. However, the lattice thermal conductivity decreased with the addition of graphene (Figure 6c). This decrease in the lattice thermal conductivity may result from three factors: the presence of oxygen vacancies, nanostructured grains, and the presence of graphene. As inferred by EBSD and XRD analysis, the LSTO and its nanocomposites were significantly reduced during their manufacture and thus contained a high concentration of oxygen vacancies. Randomly distributed and clustered oxygen vacancies would increase effective phonon scattering, thereby reducing lattice thermal conductivity.[41,42]

As discussed earlier, the introduction of graphene led to significant reduction in grain size of the nanocomposites, such that at loadings of $\geq$ 0.6 wt % graphene, the majority of grains were nanoscale with an average grain size smaller than 412 nm, compared to that of 2.2 μm for pure LSTO. It is well-known that such nanostructuring of the microstructure increases phonon scaterring.[7,22] However, above the percolation threshold, where a continuous graphene network develops, the graphene provides an effective path for phonon transfer. Thus, the lattice thermal conductivity for 1 wt % G/LSTO nanocomposite is significantly higher than that of 0.6 wt % G/LSTO nanocomposite (Figure 6c,d).

The temperature dependence of the dimensionless figure of merit ZT for the samples is shown in Figure 7, panel a; data for

DOI: 10.1021/acsami.5b03522
ACS Appl. Mater. Interfaces 2015, 7, 15898–15908

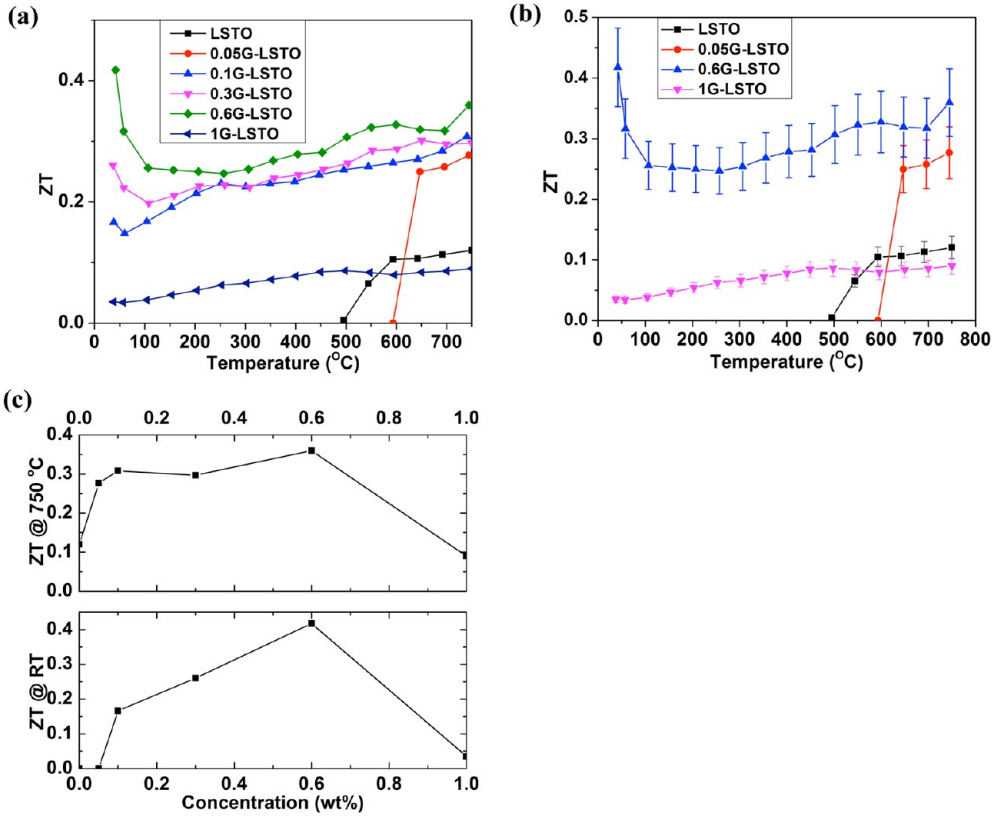

Figure 7. Thermoelectric figure of merit for LSTO and the nanocomposites: (a) *ZT* as a function of temperature, (b) *ZT* of selective samples (with uncertainty bars) as a function of temperature, and (c) *ZT* at room temperature and at 750 °C as a function of concentration of graphene. The lines are drawn as a guide to the eye. Note that there is a 15% uncertainty in all data points (shown as the error bars in panel b).

selective samples with uncertainty bars are shown in Figure 7, panel b. The pure LSTO exhibited a narrow thermal window above 500 °C, with the highest *ZT* of 0.12 at 750 °C. Similarly, the 0.05 wt % G/LSTO also showed a narrow thermal window but a superior *ZT* in excess of 0.2. With the incorporation of 0.1 wt % graphene, the nanocomposites started to show a wide thermal window throughout the whole temperature range, along with further improvement in *ZT*. The highest *ZT* of 0.42 was obtained at room temperature when 0.6 wt % graphene was added. With increasing temperature, *ZT* reduced to a minimum of 0.25 at 250 °C, followed by gradual increase to reach a secondary maximum of 0.36 at 750 °C. The high *ZT* at room temperature is due to the combination of high power factor of 2400 $\mu Wm^{-1} K^{-2}$ and low thermal conductivity of 1.8 $Wm^{-1} K^{-1}$. The relatively high power factor and low thermal conductivity also resulted in wide thermal window with *ZT* all above 0.25. Figure 7, panel b shows *ZT* at room temperature and 750 °C as a function of graphene concentration.

It is clear that *ZT* increased with the increasing graphene concentration up to 0.6 wt %, but with increased loading of graphene the thermoelectric performance was impaired. Conclusively, the incorporation of graphene in the metal oxide, which is LSTO, significantly enhanced thermoelectric performance. The incorporation of 0.6 wt % graphene gave the greatest improvement, with 281% enhancement of the minimum *ZT* compared to that of pure LSTO. As discussed above, this improvement in ZT is believed to a combination of the graphene increasing the electrical conductivity while simultaneously nanotexturing the LSTO phase, reducing the thermal conductivity. Furthermore, the nanocomposites exhibited an extraordinary broad operational thermal window compared to other thermoelectric materials and their nanocomposites with graphene.[34−38]

Prototype 7 Couple Device. A preliminary 7-couple device was fabricated using bismuth strontium cobalt oxide (BSCO) and G-LSTO pucks with each puck 3 mm high with 2.5 × 2.5 mm^2 cross-section (Figure 8). The device confirmed that the addition of graphene to LSTO does work at room temperature and significantly broadens the thermal operating window (Figure 8). Significantly, with one side at just 17 °C and the other at 267 °C, the device had an open-circuit voltage

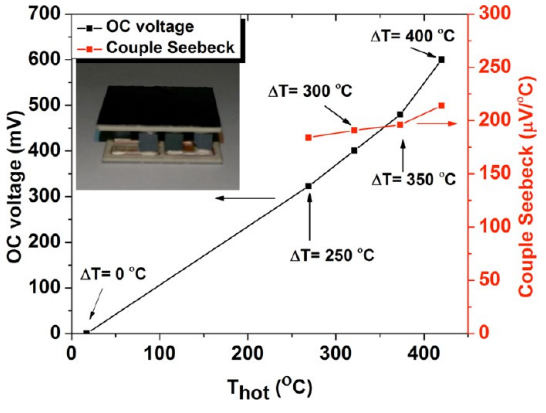

Figure 8. Performance of a thermoelectric module consisting of seven pairs of thermoelectric elements: the open-circuit voltage and couple Seebeck coefficient as a function of hot side temperature (T_{hot}); ΔT is the temperature difference across the module. The inset is a photograph of the module.

DOI: 10.1021/acsami.5b03522
ACS Appl. Mater. Interfaces 2015, 7, 15898−15908

Table 2. Test Conditions and the Resultant Performance of the Thermoelectric Device

ΔT (°C)	T_{cold} (°C)	T_{hot} (°C)	mean temperature (°C)	OC voltage (mV)	device Seebeck coefficient (μV/K)	single couple Seebeck coefficient (μV/K)
250	17	269	143	323	1290	184
300	17	321	169	401	1336	191
350	18	373	195	480	1370	196
400	19	420	219	600	1500	214

of 323 mV and a Seebeck coefficient of 1290 μV/K (Table 2). As expected, the performance improved with increasing temperature difference, with these values increasing to 600 mV and 1500 μV/K, respectively, when the hot side was raised to 420 °C.

CONCLUSIONS

A series of LSTO nanocomposites incorporated with graphene were successfully sintered by a traditional process under an Ar/H_2 atmosphere. The LSTO and its nanocomposites exhibited multiphase structures as well as strong oxygen reduction. The grain size of the nanocomposites decreased dramatically with increasing graphene concentration. The 0.6 wt % G/LSTO nanocomposite exhibited an average grain size of ~400 nm, which is five-times smaller than that of pure LSTO. The thermal conductivity of the nanocomposites also decreased with increasing concentration of graphene, up to 0.6 wt %. The significant reduction is due to effective phonon scattering induced by large numbers of oxygen vacancies, nanostructured grains, and heterointerfaces between the graphene and the grains. The incorporation of graphene significantly improved electrical conductivity and power factor; the highest electrical conductivity of 2.0×10^5 S/m was observed at room temperature. Together with a moderate Seebeck coefficient, a high power factor of ~2500 $\mu Wm^{-1} K^{-2}$ was reached at room temperature. Because of reduction in the thermal conductivity and improvement in the power factor, the figure of merit ZT was greatly enhanced with the incorporation of graphene. The best ZT was achieved when 0.6 wt % graphene was added; ZT = 0.42 at room temperature and 0.36 at 750 °C. Most significantly, the addition of graphene broadened the operational thermal window, an effect not seen with other dopants/additives. The ZT was >0.25 at room temperature to 750 °C. A prototype device achieved an open-circuit potential of 600 mV with cold side at 18.5 °C and a temperature difference of 400 °C. This discovery highlights an alternative strategy to nanostructuring for developing high-performance, environmental friendly, low cost thermoelectric materials and extending their use to lower-temperature applications such as automotive and low-temperature generators.

METHODS

Materials. The graphene was produced by exfoliating nanographite platelets (xGnP M-5) purchased from XG Sciences Ltd. All solvents were purchased from Sigma-Aldrich, UK. Cetyltrimethylammonium bromide (CTAB) was obtained from Sigma-Aldrich, UK. The molecular weight of the CTAB is 364 g/mol. The aggregation number of the CTAB is 170; the micellar average molecular weight is 62 000. The oxide starting powders of strontium titanate (5 μm), strontium carbonate, titanium dioxide, and lanthanum oxide were obtained from Sigma-Aldrich, UK.

Preparation of LSTO Ceramic Powder. LSTO ceramics of composition $La_{0.067}Sr_{0.9}TiO_3$ were produced by the following procedure. The strontium carbonate, titanium dioxide, and lanthanum oxide powders were the precursors. An excess weight of the precursor powders was dried in a furnace at 950 °C for 4 h to remove any adsorbed species. Appropriate amounts of strontium carbonate (72.2 g), titanium dioxide (43.4 g), and lanthanum oxide (5.9 g) were then weighed to yield 100-g batches of $La_{0.067}Sr_{0.9}TiO_3$ and mixed with 8 mm zirconia balls and propan-2-ol in a 1:1:1 weight ratio to create a slurry. Each batch was vibratory milled for 24 h. Subsequently, the slurry was dried at 85 °C in an oven to remove the propan-2-ol. The milled powders were transferred to an alumina crucible and calcined in a furnace for 4 h at 1100 °C, with heating/cooling rates of 180 °C hr^{-1}. The calcined powders were milled again under the same conditions as stated previously. The final powders were stored in sealed bottles until required.

Preparation of Graphene Sheets. The procedure for preparing graphene sheets followed a liquid exfoliation method developed by Lin et al.[43] Typically, 100 mg of graphite nanoplatelets (xGnp M-5) was first sonicated in a 5 mL mixture of phenol and methanol (ratio 5:1) for 30 min. Ten milligrams of CTAB was added, and the resultant suspension sonicated for another 30 min. It was then left to rest for 2 days. Afterward, the mixture was added to a 100 mL mixture of water and methanol (ratio 4:1) followed by stirring for 2 h. Finally, the resultant graphite/graphene mixture was separated by centrifugation, and the unwashed exfoliated graphene dispersion was stored at room temperature for further use.

Preparation of G/LSTO Nanocomposites. Preparation of 0.1 wt % G/LSTO is demonstrated as an example. First, 10 mL of the exfoliated graphene dispersion, which contained 10 mg of graphene (produced as described above), was sonicated for 0.5 h. At the same time, 10 g of the calcined LSTO powder was added to 100 mL of water, followed by 0.5 h sonication. Subsequently, the graphene dispersion and the LSTO water dispersion were mixed together by stirring for 0.5 h and then 0.5 h sonication. The resultant mixture was then filtered and dried at 60 °C under vacuum for 8 h. The dried powders were then milled in planetary mill at 10 000 rpm for 3 h. The resulting powders were stored in sealed bottles.

For sintering, the powders were pressed into pellets of 10 mm and 20 mm diameter with thickness between 3 and 5 mm. The pellets were placed on a bed of 5 wt % xGnp/strontium titanate powder and sintered at 1427 °C under an atmosphere of 95% argon and 5% hydrogen for 24 h. The powder bed was used as an oxygen scavenger to prevent oxidation of graphene in the main composites.

Characterization. The density (ρ) of sintered products was determined by the Archimedes method. XRD spectra of sintered and polished LSTO and its nanocomposites with graphene were obtained by use of a Philips automatic powder diffractometer (APD, copper anode at 50 kV and filament current 40 mA). The samples were scanned from 10−85° with a step size of 0.02° and a scan speed of 0.0025° s^{-1}.

The microstructures of LSTO/G nanocomposites were investigated by SEM (Philips XL30 FEGSEM). The fracture surfaces were gold coated prior to use. TEM was undertaken using a FEI Tecnai G2 TEM (200 kV). Some of the samples were mechanically crushed, dispersed in acetone, and then drops dried on a holey copper grid for direct TEM imaging. Alternatively, the solid samples were ground, then polished down by using 1 μm diamond paste followed by OPS colloidal silica (22−28 nm, pH 9−10). The grain sizes and compositions of the nanocomposites were determined by EBSD using an FEI Quanta 650 FEGSEM on polished samples.

The electrical resistivity and Seebeck coefficients of LSTO and its nanocomposites with graphene were determined simultaneously (under a helium atmosphere) from room temperature to 750 °C using a ULVAC-RIKO ZEM-3 system. Thermal diffusivity (D) was determined by the laser flash method using system designed in-house.

DOI: 10.1021/acsami.5b03522
ACS Appl. Mater. Interfaces 2015, 7, 15898−15908

The heat capacity (C_p) was measured using a TA Instruments DSC 2920 calorimeter in modulated differential scanning calorimetry (MDSC) mode. Nitrogen was used as the purge gas (40 mL/min). The samples were heated up at a rate of 3 °C/min, with modulation amplitude of 1 °C and a period of 80 s. The thermal conductivity was obtained from the relationship $\kappa = DC_p\rho$.

Prototype Device Fabrication. A 7-couple device was assembled using copper metallised ceramics as the support substrate and silver screen printing ink as the joining material. The LSTO with 0.6 wt % graphene (0.6 wt % G/LSTO) discs and BSCO (produced under separate study) discs were cut using a diamond blade saw and ground to form pellets 2.5 mm × 2.5 mm with height of 3 mm. After copper metallisation, the ceramics were polished to remove the copper oxide surface layer and cleaned with deionized water, isopropanol, and acetone. The components were air-dried. Silver ink was then applied to the copper contacts and the pellets connected to form a module; they were connected in series electrically, but in parallel thermally (Figure 8). For testing, the module was clamped in a test rig and subjected to a differential temperature.

■ ASSOCIATED CONTENT

Supporting Information

Calculation of electronic thermal conductivity (κ_e) and lattice thermal conductivity (κ_L). Measured densities of LSTO and its nanocomposites with graphene. Raman spectra of graphene and 0.6 wt % graphene/LSTO nanocomposite. The Supporting Information is available free of charge on the ACS Publications website at DOI: 10.1021/acsami.5b03522.

■ AUTHOR INFORMATION

Corresponding Authors

*E-mail: Rober.Freer@manchester.ac.uk.
*E-mail: Ian.Kinloch@manchester.ac.uk.

Notes

The authors declare the following competing financial interest(s): The University has filed a patent on graphene in thermoelectric materials.

■ ACKNOWLEDGMENTS

This work was supported by The University of Manchester Intellectual Properties (UMIP), Engineering and Physical Sciences Research Council (EPSRC, EP/I023879/1), and the European Union Seventh Framework Programme under Grant agreement No. 604391 Graphene Flagship.

■ REFERENCES

(1) Ohta, H. Thermoelectrics Based on Strontium Titanate. *Mater. Today* **2007**, *10*, 44−49.
(2) Biswas, K.; He, J. Q.; Blum, I. D.; Wu, C. I.; Hogan, T. P.; Seidman, D. N.; Dravid, V. P.; Kanatzidis, M. G. High-Performance Bulk Thermoelectrics with All-Scale Hierarchical Architectures. *Nature* **2012**, *489*, 414−418.
(3) Poudel, B.; Hao, Q.; Ma, Y.; Lan, Y. C.; Minnich, A.; Yu, B.; Yan, X. A.; Wang, D. Z.; Muto, A.; Vashaee, D.; Chen, X. Y.; Liu, J. M.; Dresselhaus, M. S.; Chen, G.; Ren, Z. F. High-Thermoelectric Performance of Nanostructured Bismuth Antimony Telluride Bulk Alloys. *Science* **2008**, *320*, 634−638.
(4) Zhao, L.-D.; Lo, S.-H.; Zhang, Y.; Sun, H.; Tan, G.; Uher, C.; Wolverton, C.; Dravid, V. P.; Kanatzidis, M. G. Ultralow Thermal Conductivity and High Thermoelectric Figure of Merit in SnSe Crystals. *Nature* **2014**, *508*, 373−377.
(5) Koumoto, K.; Funahashi, R.; Guilmeau, E.; Miyazaki, Y.; Weidenkaff, A.; Wang, Y. F.; Wan, C. L. Thermoelectric Ceramics for Energy Harvesting. *J. Am. Ceram. Soc.* **2013**, *96*, 1−23.
(6) Koumoto, K.; Wang, Y. F.; Zhang, R. Z.; Kosuga, A.; Funahashi, R. Oxide Thermoelectric Materials: A Nanostructuring Approach. *Annu. Rev. Mater. Res.* **2010**, *40*, 363−394.
(7) Wan, C. L.; Wang, Y. F.; Wang, N.; Norimatsu, W.; Kusunoki, M.; Koumoto, K. Development of Novel Thermoelectric Materials by Reduction of Lattice Thermal Conductivity. *Sci. Technol. Adv. Mater.* **2010**, *11*, 044306.
(8) Zhao, L. D.; Zhang, B. P.; Liu, W. S.; Li, J. F. Effect of Mixed Grain Sizes on Thermoelectric Performance of Bi_2Te_3 Compound. *J. Appl. Phys.* **2009**, *105*, 023704.
(9) Pei, Y. L.; He, J. Q.; Li, J. F.; Li, F.; Liu, Q. J.; Pan, W.; Barreteau, C.; Berardan, D.; Dragoe, N.; Zhao, L. D. High Thermoelectric Performance of Oxyselenides: Intrinsically Low Thermal Conductivity of Ca-Doped BiCuSeO. *NPG Asia Mater.* **2013**, *5*, e47.
(10) Lan, Y. C.; Minnich, A. J.; Chen, G.; Ren, Z. F. Enhancement of Thermoelectric Figure-of-Merit by a Bulk Nanostructuring Approach. *Adv. Funct. Mater.* **2010**, *20*, 357−376.
(11) Kraemer, D.; Poudel, B.; Feng, H. P.; Caylor, J. C.; Yu, B.; Yan, X.; Ma, Y.; Wang, X. W.; Wang, D. Z.; Muto, A.; McEnaney, K.; Chiesa, M.; Ren, Z. F.; Chen, G. High-Performance Flat-Panel Solar Thermoelectric Generators with High Thermal Concentration. *Nat. Mater.* **2011**, *10*, 532−538.
(12) Fergus, J. W. Oxide Materials for High Temperature Thermoelectric Energy Conversion. *J. Eur. Ceram. Soc.* **2012**, *32*, 525−540.
(13) Walia, S.; Balendhran, S.; Nili, H.; Zhuiykov, S.; Rosengarten, G.; Wang, Q. H.; Bhaskaran, M.; Sriram, S.; Strano, M. S.; Kalantar-zadeh, K. Transition Metal Oxides—Thermoelectric Properties. *Prog. Mater. Sci.* **2013**, *58*, 1443−1489.
(14) Backhaus-Ricoult, M.; Rustad, J.; Moore, L.; Smith, C.; Brown, J. Semiconducting Large Bandgap Oxides as Potential Thermoelectric Materials for High-Temperature Power Generation? *Appl. Phys. A-Mater.* **2014**, *116*, 433−470.
(15) Wang, H. C.; Wang, C. L.; Su, W. B.; Liu, J. A.; Sun, Y.; Peng, H.; Mei, L. A. M. Doping Effect of La and Dy on the Thermoelectric Properties of SrTiO3. *J. Am. Ceram. Soc.* **2011**, *94*, 838−842.
(16) Zhang, L. H.; Tosho, T.; Okinaka, N.; Akiyama, T. Thermoelectric Properties of Combustion-Synthesized Lanthanum-Doped Strontium Titanate. *Mater. Trans.* **2007**, *48*, 1079−1083.
(17) Ohta, S.; Nomura, T.; Ohta, H.; Koumoto, K. High-Temperature Carrier Transport and Thermoelectric Properties of Heavily La- or Nb-Doped $SrTiO_3$ Single Crystals. *J. Appl. Phys.* **2005**, *97*, 034106.
(18) Ohta, S.; Ohta, H.; Koumoto, K. Grain Size Dependence of Thermoelectric Performance of Nb-Doped $SrTiO_3$ Polycrystals. *J. Ceram. Soc. Jpn.* **2006**, *114*, 102−105.
(19) Ohta, S.; Nomura, T.; Ohta, H.; Hirano, M.; Hosono, H.; Koumoto, K. Large Thermoelectric Performance of Heavily Nb-Doped $SrTiO_3$ Epitaxial Film at High Temperature. *Appl. Phys. Lett.* **2005**, *87*, 092108.
(20) Kumar, S. R. S.; Barasheed, A. Z.; Alshareef, H. N. High Temperature Thermoelectric Properties of Strontium Titanate Thin Films with Oxygen Vacancy and Niobium Doping. *ACS Appl. Mater. Interfaces* **2013**, *5*, 7268−7273.
(21) Dang, F.; Wan, C. L.; Park, N. H.; Tsuruta, K.; Seo, W. S.; Koumoto, K. Thermoelectric Performance of $SrTiO_3$ Enhanced by Nanostructuring-Self-Assembled Particulate Film of Nanocubes. *ACS Appl. Mater. Interfaces* **2013**, *5*, 10933−10937.
(22) Wang, Y. F.; Fujinami, K.; Zhang, R. Z.; Wan, C. L.; Wang, N.; Ba, Y. S.; Koumoto, K. Interfacial Thermal Resistance and Thermal Conductivity in Nanograined $SrTiO_3$. *Appl. Phys. Express* **2010**, *3*, 031101.
(23) Wang, N.; Chen, H. J.; He, H. C.; Norimatsu, W.; Kusunoki, M.; Koumoto, K. Enhanced Thermoelectric Performance of Nb-Doped $SrTiO_3$ by Nano-Inclusion with Low Thermal Conductivity. *Sci. Rep. UK* **2013**, *3*, 3449.
(24) Okuda, T.; Nakanishi, K.; Miyasaka, S.; Tokura, Y. Large Thermoelectric Response of Metallic Perovskites: $Sr_{1-x}La_xTiO_3$ ($0 \le x \le 0.1$). *Phys. Rev. B* **2001**, *63*, 113104.

DOI: 10.1021/acsami.5b03522
ACS Appl. Mater. Interfaces 2015, 7, 15898−15908

(25) Lee, C.; Wei, X. D.; Kysar, J. W.; Hone, J. Measurement of the Elastic Properties and Intrinsic Strength of Monolayer Graphene. *Science* **2008**, *321*, 385−388.
(26) Saito, K.; Nakamura, J.; Natori, A. Ballistic Thermal Conductance of a Graphene Sheet. *Phys. Rev. B* **2007**, *76*, 115409.
(27) Wu, Z. S.; Ren, W. C.; Gao, L. B.; Zhao, J. P.; Chen, Z. P.; Liu, B. L.; Tang, D. M.; Yu, B.; Jiang, C. B.; Cheng, H. M. Synthesis of Graphene Sheets with High Electrical Conductivity and Good Thermal Stability by Hydrogen Arc Discharge Exfoliation. *ACS Nano* **2009**, *3*, 411−417.
(28) Dragoman, D.; Dragoman, M. Giant Thermoelectric Effect in Graphene. *Appl. Phys. Lett.* **2007**, *91*, 203116.
(29) Morozov, S. V.; Novoselov, K. S.; Katsnelson, M. I.; Schedin, F.; Elias, D. C.; Jaszczak, J. A.; Geim, A. K. Giant Intrinsic Carrier Mobilities in Graphene And Its Bilayer. *Phys. Rev. Lett.* **2008**, *100*, 016602.
(30) Allen, M. J.; Tung, V. C.; Kaner, R. B. Honeycomb Carbon: A Review of Graphene. *Chem. Rev.* **2010**, *110*, 132−145.
(31) Novoselov, K. S.; Geim, A. K.; Morozov, S. V.; Jiang, D.; Zhang, Y.; Dubonos, S. V.; Grigorieva, I. V.; Firsov, A. A. Electric Field Effect in Atomically Thin Carbon Films. *Science* **2004**, *306*, 666−669.
(32) Novoselov, K. S.; Morozov, S. V.; Mohinddin, T. M. G.; Ponomarenko, L. A.; Elias, D. C.; Yang, R.; Barbolina, I. I.; Blake, P.; Booth, T. J.; Jiang, D.; Giesbers, J.; Hill, E. W.; Geim, A. K. Electronic Properties of Graphene. *Phys. Status Solidi B* **2007**, *244*, 4106−4111.
(33) Novoselov, K. S.; Geim, A. K.; Morozov, S. V.; Jiang, D.; Katsnelson, M. I.; Grigorieva, I. V.; Dubonos, S. V.; Firsov, A. A. Two-Dimensional Gas of Massless Dirac Fermions in Graphene. *Nature* **2005**, *438*, 197−200.
(34) Feng, B.; Xie, J.; Cao, G. S.; Zhu, T. J.; Zhao, X. B. Enhanced Thermoelectric Properties of P-Type $CoSb_3$/Graphene Nanocomposite. *J. Mater. Chem. A* **2013**, *1*, 13111−13119.
(35) Dong, J. D.; Liu, W.; Li, H.; Su, X. L.; Tang, X. F.; Uher, C. In Situ Synthesis and Thermoelectric Properties of PbTe-Graphene Nanocomposites by Utilizing a Facile and Novel Wet Chemical Method. *J. Mater. Chem. A* **2013**, *1*, 12503−12511.
(36) Xu, K. L.; Chen, G. M.; Qiu, D. Convenient Construction of Poly(3,4-ethylenedioxythiophene)-Graphene Pie-like Structure with Enhanced Thermoelectric Performance. *J. Mater. Chem. A* **2013**, *1*, 12395−12399.
(37) Abad, B.; Alda, I.; Diaz-Chao, P.; Kawakami, H.; Almarza, A.; Amantia, D.; Gutierrez, D.; Aubouy, L.; Martin-Gonzalez, M. Improved Power Factor of Polyaniline Nanocomposites with Exfoliated Graphene Nanoplatelets (GNPs). *J. Mater. Chem. A* **2013**, *1*, 10450−10457.
(38) Xiang, J. L.; Drzal, L. T. Templated Growth of Polyaniline on Exfoliated Graphene Nanoplatelets (GNP) and Its Thermoelectric Properties. *Polymer* **2012**, *53*, 4202−4210.
(39) Howard, S. A.; Yau, J. K.; Anderson, H. U. Structural Characteristics of $Sr_{1-x}La_xTi_{3\pm\delta}$ as a Function of Oxygen Partial-Pressure at 1400-Degrees-C. *J. Appl. Phys.* **1989**, *65*, 1492−1498.
(40) Jung, W. H. Structure, Thermopower, and Electrical Transport Properties of $La_{2/3}TiO_{3-\delta}$. *J. Mater. Sci. Lett.* **1999**, *18*, 1181−1183.
(41) Muller, D. A.; Nakagawa, N.; Ohtomo, A.; Grazul, J. L.; Hwang, H. Y. Atomic-Scale Imaging of Nanoengineered Oxygen Vacancy Profiles in $SrTiO_3$. *Nature* **2004**, *430*, 657−661.
(42) Yu, C.; Scullin, M. L.; Huijben, M.; Ramesh, R.; Majumdar, A. Thermal Conductivity Reduction in Oxygen-Deficient Strontium Titanates. *Appl. Phys. Lett.* **2008**, *92*, 191911.
(43) Lin, Y.; Jin, J.; Kusmartsevab, O.; Song, M. Preparation of Pristine Graphene Sheets and Large-Area/Ultrathin Graphene Films for High Conducting and Transparent Applications. *J. Phys. Chem. C* **2013**, *117*, 17237−17244.

DOI: 10.1021/acsami.5b03522
ACS Appl. Mater. Interfaces 2015, 7, 15898−15908